

Local Fourier Slice Photography

CHRISTIAN LESSIG*, Institute for Simulation and Graphics, Otto-von-Guericke-Universität Magdeburg, Germany

Light field cameras provide intriguing possibilities, such as post-capture refocus or the ability to look behind an object. This comes, however, at the price of significant storage requirements. Compression techniques can be used to reduce these but refocusing and reconstruction require so far again a dense representation. To avoid this, we introduce a sheared local Fourier slice equation that allows for refocusing directly from a compressed light field, either to obtain an image or a compressed representation of it. The result is made possible by wavelets that respect the “slicing’s” intrinsic structure and enable us to derive exact reconstruction filters for the refocused image in closed form. Image reconstruction then amounts to applying these filters to the light field’s wavelet coefficients, and hence no decompression is necessary. We demonstrate that this substantially reduces storage requirements and also computation times. We furthermore analyze the computational complexity of our algorithm and show that it scales linearly with the size of the reconstructed region and the non-negligible wavelet coefficients, i.e. with the visual complexity.

CCS Concepts: • **Computing methodologies** → **Computational photography**; *Image compression*; • **Mathematics of computing** → *Computation of transforms*.

Additional Key Words and Phrases: light field camera, Fourier slice theorem, wavelets

ACM Reference Format:

Christian Lessig. 2019. Local Fourier Slice Photography. 1, 1 (December 2019), 12 pages. <https://doi.org/10.1145/1122445.1122456>

1 INTRODUCTION

Light field cameras, which record the full four-dimensional light field, open up many possibilities for both consumer, e.g. [Ng et al. 2005], and professional applications, e.g. [Levoy et al. 2006]. Prime examples are post-capture refocus and the ability to obtain images where every depth is in focus. These possibilities, however, come at the price of significant storage requirements. Compression techniques can be used to alleviate these but most processing tasks require again a dense representation of the light field.

To avoid this, we propose *local Fourier slice photography* that enables the computation of refocused images directly from a light field’s compressed representation. Our work draws inspiration from Ng’s seminal Fourier slice photography [2005] that performs image reconstruction in the frequency domain using the projection slice theorem. We combine Ng’s work with a recent extension of the slice theorem [Lessig 2018a] that employs carefully chosen

wavelets to allow for projection from a compressed representation. We generalize the latter and derive a *sheared, local projection slice equation* that yields exact, shear-dependent reconstruction kernels for the projected signal. Using these on a light field’s wavelet coefficients enables the reconstruction of refocused images directly from a compressed representation. We also derive an extension of the sheared, local projection slice equation that enables one to directly obtain compressed images. Our experimental results confirm that our approach yields high fidelity, refocused images with significantly reduced storage requirements and that at high compression rates errors mainly manifest themselves through lost high-frequency detail, i.e. without distracting artifacts.

The sparsity that reduces storage requirements also reduces computational costs. We show this experimentally and verify it through a theoretical analysis that establishes a linear dependence on the number of nonzero coefficients. Because of the spatial localization of the wavelets, the costs of our technique depend on the light field’s angular resolution, which was not the case for Fourier Slice Photography [Ng 2005]. However, in Ng’s work one cannot easily take advantage of redundancy in the data and the localization also enables us to obtain all-focus images, which is not possible using Fourier slice photography.

A conceptual overview of our approach is provided in Fig. 1 and the computations required in an implementation are summarized in Algo. 1. The remainder of the paper, which expounds the details, is structured as follows. After reviewing related work in the next subsection, we provide in Sec. 2 the necessary background on the wavelets we use. In Sec. 3 we derive the sheared local Fourier slice equation and develop our technique to obtain a refocused image directly from a light field’s compressed representation. Experimental results on refocused image reconstruction and all-focus images as well as details on our reference implementation are presented in Sec. 4. We conclude in Sec. 5 with a discussions of possible directions for future work.

1.1 Related Work

Although initially confined to synthetic images [Chai et al. 2000; Gortler et al. 1996; Levoy and Hanrahan 1996], in the 2000s practical means to capture real-world light field data sets became available [Ng et al. 2005; Venkataraman et al. 2013; Wilburn et al. 2005]. With these, the generation, processing, and display of light fields has become an important research direction [Ihrke et al. 2016; Wu et al. 2017]. In the following, we therefore will focus on related work most pertinent to our own.

Ng [2005] showed that post-capture refocus can be formulated in the frequency domain using the Fourier projection slice theorem and that this provides an asymptotic speedup compared to the pixel-domain. Our work is inspired by Ng’s and we combine it with a recent result in optics [Lessig 2018a] that extends the projection slice theorem to a spatially localized form using wavelets. The extension relies on the use of polar wavelets, which is a recently

Author’s address: Christian Lessig, lessig@isg.cs.uni-magdeburg.de, Institute for Simulation and Graphics, Otto-von-Guericke-Universität Magdeburg, Universitätsplatz 2, Magdeburg, 39106, Germany.

Permission to make digital or hard copies of all or part of this work for personal or classroom use is granted without fee provided that copies are not made or distributed for profit or commercial advantage and that copies bear this notice and the full citation on the first page. Copyrights for components of this work owned by others than the author(s) must be honored. Abstracting with credit is permitted. To copy otherwise, or republish, to post on servers or to redistribute to lists, requires prior specific permission and/or a fee. Request permissions from permissions@acm.org.

© 2019 Copyright held by the owner/author(s). Publication rights licensed to ACM. XXXX-XXXX/2019/12-ART \$15.00 <https://doi.org/10.1145/1122445.1122456>

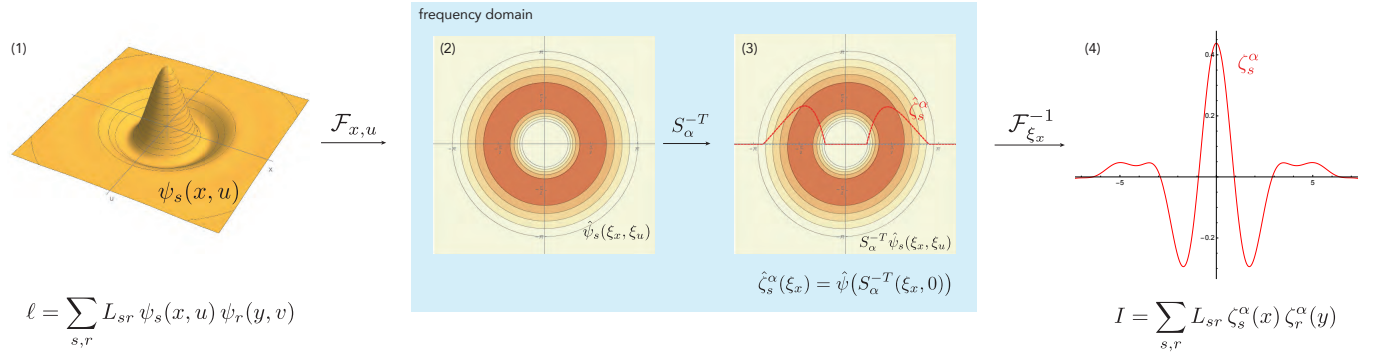


Fig. 1. Overview of our approach: (1) A light field $\ell(x, y, u, v)$ in the two plane parameterization is represented using polar wavelets $\psi_s(x, u)$ and $\psi_r(y, v)$, exploiting the separability of the refocusing problem. (2) The wavelets are defined in polar coordinates in the Fourier domain. They are hence naturally compatible with the restriction to a line through the origin which implements refocused image reconstruction in the Fourier domain [Ng 2005]. (3) The restriction of the sheared polar wavelet $\hat{\psi}_s(S_\alpha^{-T}(\xi_x, \xi_u))$ to the ξ_x axis defines the one dimensional wavelet $\hat{\zeta}_s^\alpha(\xi_x) = \hat{\psi}_s(S_\alpha^{-T}(\xi_x, 0))$ (and analogous for (y, v)). (4) The inverse Fourier transform of $\hat{\zeta}_s^\alpha(\xi_x)$, which can be computed in closed form, provides the exact, spatial reconstruction filters to obtain a refocused image from the wavelet coefficients ℓ_{sr} of the light field.

introduced family of wavelets defined separably in polar coordinates in the Fourier domain [Unser and Chenouard 2013; Unser et al. 2011; Unser and Van De Ville 2010]. The family includes a wide range of steerable wavelets [Freeman and Adelson 1991; Perona 1991; Simoncelli and Freeman 1995] as well as curvelets [Candès and Donoho 2005a,b] and ridgelets [Candès and Donoho 1999; Donoho 2000], the latter ones providing quasi-optimally sparse representations of two dimensional, image-like signals [Candès and Donoho 2004; Donoho 2000]. Our work also uses polar wavelets and exploits their separability in polar coordinates in the frequency domain; it benefits from the sparsity available with curvelet-like constructions.

Light field imaging in the Fourier domain was also considered by Shi et al. [2014]. Their motivation was to circumvent the sparsity degradation that results when the discrete instead of the continuous Fourier transform is used in numerical calculations. This does not occur for us since our reconstruction kernels are obtained in the continuous domain. Furthermore, while Shi et al. require a nonlinear optimization to obtain sparsity we use simple thresholding and rely on the structure of natural images in frequency space [Mallat 2009, Ch. 9]. The frequency representation of light fields has also been considered by Liang and Ramamoorthi [2015]. These authors provide a comprehensive analysis of the trade-offs involved in the design of light field cameras and their sensors. This work is orthogonal to ours, however, since we assume we have a preprocessed light field data set as input.

Learning-based techniques for the reconstruction of images from light field data have also been considered in recent work, e.g. [Kalanitari et al. 2016; Levin et al. 2008; Xu et al. 2018; Yoon et al. 2015]. The objective there is typically to perform the reconstruction from a reduced set of measurements, which incurs much higher computational costs. We believe that the polar wavelet representation of a light field that we employ in our work provides a useful pre-processing for learning-based reconstruction since it removes redundancy while respecting the intrinsic structure of the task.

A variety of approaches for the compression of light field data sets have been proposed in the literature [Viola et al. 2017; Wu et al. 2017], for example adapting techniques used for image compression, e.g. [Alves et al. 2018]; developing custom ones for slices or the full 4D light field, e.g. [Aggoun 2006; Aggoun and Mazri 2008; Conti et al. 2014; Kundu 2012]; or extending video compression schemes by exploiting that a light field can be seen as a sequence of images recorded from a set of nearby vantage points, e.g. [Dai et al. 2015; Vieira et al. 2015]. Our use of polar wavelet for transform coding is dictated by our objective to refocus from the compressed representation. Furthermore, while we attain compression rates comparable to those reported in the literature [Viola et al. 2017; Wu et al. 2017], we do not provide a full compressions technique, e.g. we do not consider the choice of color space, gamma correction, and quantization.

2 POLAR WAVELETS

Polar wavelets are defined separably in polar coordinates in the Fourier domain using a compactly supported radial window $\hat{h}(|\xi|)$, which controls the overall frequency localization, and an angular one, $\hat{\psi}(\xi)$, which controls the directionality, with $\bar{\xi} = \xi/|\xi|$. The mother wavelet is thus given by $\hat{\psi}(\xi) = \hat{\psi}(\bar{\xi})\hat{h}(|\xi|)$, cf. Fig. 2, left with the whole family of functions being generated by dilation, translation and rotation.

The angular window $\hat{\psi}(\bar{\xi})$ is conveniently described using a Fourier series. A polar wavelet is then given by

$$\hat{\psi}_s(\xi) \equiv \hat{\psi}_{jkt}(\xi) = \frac{2^j}{2\pi} \left(\sum_n \beta_{j,n}^t e^{in\theta_{\bar{\xi}}} \right) \hat{h}(2^{-j}|\xi|) e^{-i\langle \bar{\xi}, 2^j k \rangle} \quad (1)$$

with the $\beta_{j,n}^t$ controlling the angular localization. In the simplest case, $\beta_n = \delta_{n0}$ and one has isotropic, bump-like wavelet functions, cf. Fig. 1, left. Conversely, when the support of the $\beta_{j,n}^t$ is over all integers \mathbb{Z} then one can describe angular windows that are compactly supported in the polar angle $\theta_{\bar{\xi}}$. Eq. 1 then encompasses ridgelets [Candès and Donoho 1999; Donoho 2000] and second generation curvelets [Candès and Donoho 2005b], cf. Fig. 2, right.

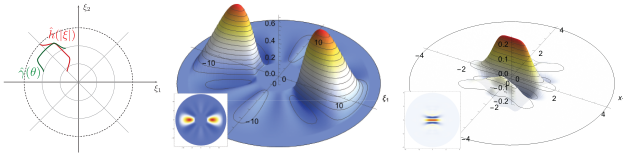


Fig. 2. *Left*: Conceptual construction of polar wavelets using window functions separable in polar coordinates. *Right*: Directional, curvelet-like polar wavelets in the frequency domain (middle) and the spatial domain (right).

A beneficial property of polar wavelets is that their spatial representation, given by the inverse Fourier transform of Eq. 1, can be computed in closed form. Using the Fourier transform in polar coordinates one obtains [Lessig 2018b]

$$\psi_s(x) \equiv \psi_{jkt}(x) = \frac{2^j}{2\pi} \sum_n i^n \beta_{j,n}^t e^{in\theta_x} h_n(|2^j x - k|) \quad (2)$$

where $h_n(|x|)$ is the Hankel transform of $\hat{h}(|\xi|)$ of order n . For $\hat{h}(|\xi|)$ we employ the window proposed for the steerable pyramid [Freeman and Adelson 1991; Portilla and Simoncelli 2000] since $h_n(|x|)$ then has a closed form expression [Lessig 2018b]. Note that the angular localization of the wavelets, which is described by the $\beta_{j,n}^t$ in Eq. 1 and Eq. 2, is invariant under the Fourier transform and only modified by the factor of $i^n = e^{in\pi/2}$ that implements a rotation by $\pi/2$.

When the polar wavelets in Eq. 2 are suitably augmented using scaling functions $\phi_{j,k}(x)$ to represent a signal's low frequency part, with $\psi_{-1,k}(x) \equiv \phi_{0,k}(x)$, then they provide a Parseval tight frame for $L_2(\mathbb{R}^2)$. Thus any function $f(x) \in L_2(\mathbb{R}^2)$ can be represented as [Unser and Chenouard 2013]

$$f(x) = \sum_{j=-1}^{\infty} \sum_{k \in \mathbb{Z}^2} \sum_{t=1}^{N_j} \underbrace{\langle f(y), \psi_{jkt}(y) \rangle}_{f_{jkt}} \psi_{jkt}(x). \quad (3)$$

Although the above frame is redundant, since it is Parseval tight it still affords most of the conveniences of an orthonormal basis, e.g. the primary and dual frame functions coincide and the norm of the signal equals those of the expansion coefficients. For an isotropic frame the redundancy is thereby $1 + 1/4 + 1/4^2 + \dots = 4/3$ and it increases when directional basis functions are used, although this typically also yields sparser representations.

Since the definition of polar wavelets in the frequency domain uses a compactly supported radial window $\hat{h}(|\xi|)$, the wavelets have non-compact support in space. Thus, a finite signal representation is not exact, since it requires a truncation of the basis functions. Nonetheless, with a sufficiently large apron region around an image, an arbitrary accuracy can be attained; in our experiments typically 4 suffices to meet the requirements of optical applications. To obtain the wavelet representation of a signal, we compute it using a coarse-to-fine, fast wavelet transform-like algorithm where on each level the computations can either be performed using discrete convolutions with filter taps in the spatial domain or by multiplication with the windows in the frequency domain.

To simplify notation, we will typically employ the multi-index $s = (j, k, t)$ and, when confusion might arise, write $s = (j_s, k_s, t_s)$.

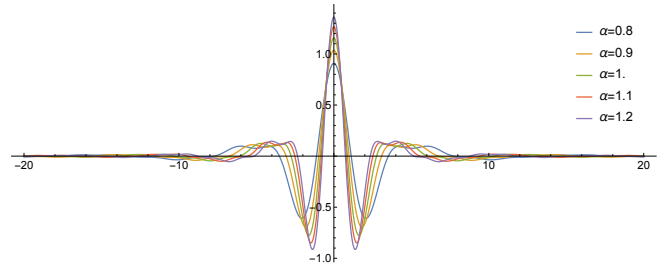


Fig. 3. Reconstruction kernel $\xi_s^{\alpha,0}(x)$ in Eq. 12 for different values of α .

The index s runs over the set \mathcal{S} that a priori includes all scales, translations, and orientations. The cardinality of a set will be denoted by $|\cdot|$, e.g. $|\mathcal{S}|$.

3 A SHEARED LOCAL FOURIER SLICE EQUATION FOR COMPUTATIONAL IMAGING

In this section we derived our image reconstruction technique. We begin by fixing notation and recalling the image formation model. At the end we analyze the computational complexity of the technique as well as sources of error.

3.1 Image Reconstruction Model

We use the two-plane parametrization for the light field $\ell(x, y, u, v)$ with (x, y) being the coordinates on the image plane and (u, v) those on the lens. We also assume $\ell(x, y, u, v)$ is non-zero only over the camera sensor in (x, y) and over the lens in (u, v) and that it already contains the $\cos(\theta)^4/F^2$ foreshortening factor where θ is the angle between the ray and the image plane normal.

For image formation we use the same model as [Ng 2005], see Fig. 4, with the image $I(x, y)$ being obtained from the light field as

$$I(x, y) = \frac{1}{\alpha^2} \int \int \ell(x/\alpha + (1-1/\alpha)u, y/\alpha + (1-1/\alpha)v, u, v) du dv$$

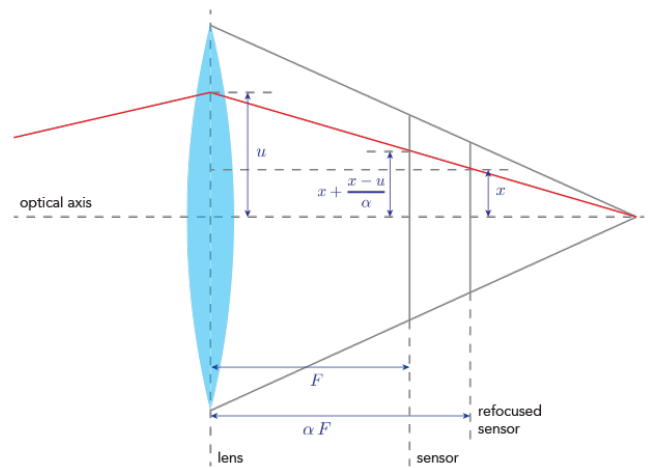


Fig. 4. Image formation model used in our work.

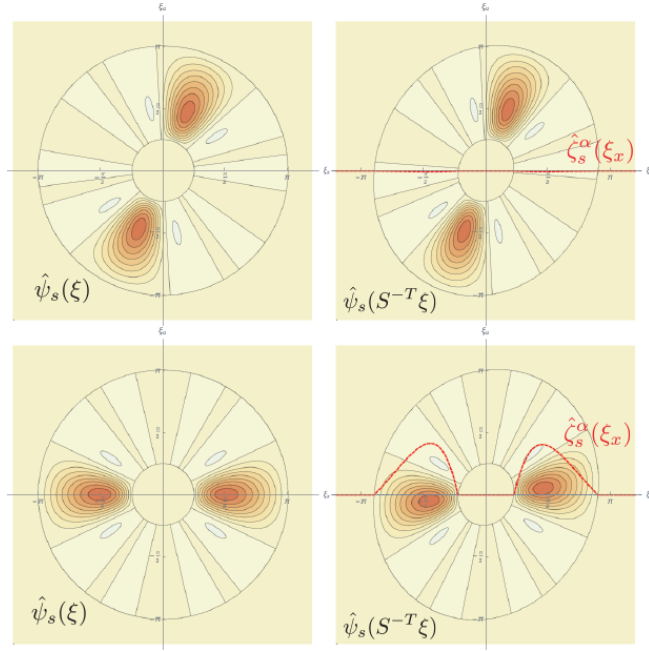


Fig. 5. Contour plots of curvelet-like, directional polar wavelets in the frequency domain at two different orientations (different rows) and with and without shear (different columns) for $\alpha = 0.9$. Shown are also the sheared reconstruction filters ζ_s^α . It is apparent that only those $\hat{\psi}_s(x)$ with an orientation close to the ξ_x -axis (dashed grey), i.e. to the slicing direction, yield ζ_s^α that contribute to the projected signal.

where α is the refocusing parameter and $\alpha = 1$ yields the original image. By changing the notation for the light field to $\ell(x, u; y, v)$, the last equation can be written more compactly as

$$I(x, y) = \int_{\mathbb{R}_u} \int_{\mathbb{R}_v} \ell(S_\alpha(x, u)^T; S_\alpha(x, u)^T) du dv \quad (4)$$

where the shear matrix S_α is given by

$$S_\alpha = \begin{pmatrix} 1/\alpha & 1 - 1/\alpha \\ 0 & 1 \end{pmatrix}; \quad (5)$$

the shear amounts to the transport of the light field in the camera from the original sensor location to the refocused one [Chai et al. 2000; Durand et al. 2005].

To obtain a form of the light field $\ell(x, u; y, v)$ that is amenable to compression, e.g. by thresholding small coefficients, we represent it in the polar wavelets introduced in Sec. 2. When we also respect the separable structure of the refocusing in Eq. 4, that is when one transform is performed over $x-u$ and the second one over $y-v$, we obtain

$$\ell(x, u; y, v) = \sum_{(s,r) \in \mathcal{L}} \ell_{sr} \psi_s(x, u) \psi_r(y, v). \quad (6)$$

Inserting this representation into Eq. 4 yields

$$I(x, y) = \iint \sum_{(s,r) \in \mathcal{L}} \ell_{sr} \psi_s(S_\alpha(x, u)^T) \psi_r(S_\alpha(y, v)^T) du dv \quad (7)$$

$$= \sum_{(s,r) \in \mathcal{L}} \ell_{sr} \int_{\mathbb{R}_u} \psi_s(S_\alpha(x, u)^T) du \int_{\mathbb{R}_v} \psi_r(S_\alpha(y, v)^T) dv$$

which shows that it suffices to determine the effect of the sheared projection for the basis functions and that this can be done independently for ψ_s and ψ_r . We will hence next study general, two-dimensional sheared projection using polar wavelets, which will yield our sheared local Fourier slice equation, before returning to imaging in Sec. 3.3.

3.2 A Sheared Local Fourier Slice Equation

We consider the sheared projection problem for the two dimensional signal $f(x, u)$ given by

$$g(x) = \int_{\mathbb{R}_u} f(S_\alpha(x, u)^T) du. \quad (8)$$

When $f(x, u)$ is represented in polar wavelets the equation becomes

$$g(x) = \sum_{s \in \mathcal{S}} f_s \int_{\mathbb{R}_u} \psi_s(S_\alpha(x, u)^T) du \quad (9)$$

To obtain a numerically practical solution to Eq. 9, we will, inspired by Ng's work [2005], consider it in the Fourier domain; a depiction of our approach is shown in Fig. 1. This yields

$$\int_{\mathbb{R}_u} \psi_s(S_\alpha(x, u)^T) du = \mathcal{F}_x^{-1} \left(\alpha^{-1} \hat{\psi}_s(S_\alpha^{-T}(\xi_x, \xi_u)^T|_{\xi_u=0}) \right) \quad (10)$$

where $S_\alpha^{-T}(\xi_x, \xi_u)^T|_{\xi_u=0}$ is a linear slice in ξ_x - ξ_u frequency space. By expanding $\hat{\psi}_s$ using the definition in Eq. 1, defining $\xi_0 = (\xi_x, 0)^T$, and writing out the inverse Fourier transform we obtain

$$\int_{\mathbb{R}_u} \psi_s(S_\alpha(x, u)^T) du = \frac{2^j \alpha^{-1}}{(2\pi)^{3/2}} \sum_n \beta_{j,n}^t \times \underbrace{\int_{\mathbb{R}_{\xi_x}} e^{in\theta} s_\alpha^{-T} \xi_0 \hat{h}(2^{-j} |S_\alpha^{-T} \xi_0|) e^{-i\langle \xi_x, 2^j S^{-1} k_s \rangle} e^{i\langle \xi_x, x \rangle} d\xi_x}_{\zeta_s^{\alpha,n}(x) = \zeta_{j_s, t_s}^{\alpha,n}(x - P_x(2^j S^{-1} k_s))} \quad (11)$$

that is, $\zeta_n^{s,\alpha}(x)$ is the inverse Fourier transform of the ξ_x -dependent term. Importantly, for our choice of the radial window the $\zeta_n^{s,\alpha}(x)$ have a closed form expression, see Appendix A, and the above equation can hence be realized numerically. Furthermore, the original shift k_s of ψ_s becomes after slicing $P_x(2^{-j} S^{-1} k_s)$, where P_x is the projection onto the x -axis. This means the shape of the $\zeta_n^{s,\alpha}(x)$ remains independent of k_s . Eq. 11 also shows that the angular localization coefficients $\beta_{j,n}^t$ are invariant under the inverse Fourier transform and the sheared projection of an arbitrary polar wavelet $\psi_x(x)$ is thus

$$\zeta_s^\alpha(x) \equiv \frac{2^j \alpha^{-1}}{(2\pi)^{3/2}} \sum_n \beta_{j,n}^t \zeta_s^{\alpha,n}(x) = \int_{\mathbb{R}_u} \psi_s(S_\alpha(x, u)^T) du. \quad (12)$$

Inserting Eq. 12 into Eq. 9 we obtain

$$g(x) = \int_{\mathbb{R}_u} f(S_\alpha(x, u)^T) du = \sum_{s \in \mathcal{S}} f_s \zeta_s^\alpha(x) \quad (13)$$

which is our sheared local Fourier slice equation with the $\zeta_s^\alpha(x)$ being the reconstruction filters that implement projection directly from the wavelet representation. A simple verification of Eq. 15 for a

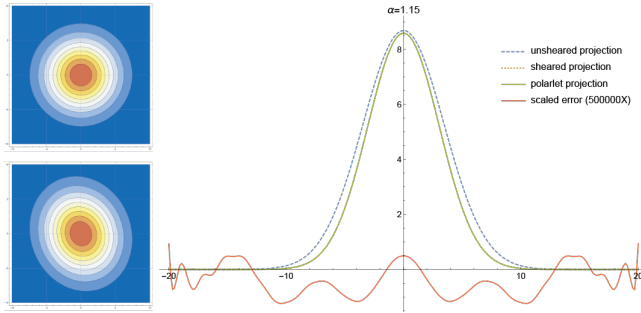


Fig. 6. Projection of sheared 2D Gaussian (left, bottom). The maximum error with the sheared local Fourier slice equation is 1.86×10^{-6} .

two dimensional Gaussian, for which the ground truth has a closed form solution, is provided in Fig. 6.

The reconstruction kernels $\zeta_s^\alpha(x)$ are wavelet-like in that they are compactly supported in the frequency domain around $\xi_x = 2^{j_s}$, since they result as a slice of a compactly supported wavelet centered at this frequency, cf. Fig. 5. They are also well localized in the spatial domain, since the sliced window has the same decay as $\hat{\psi}_s(\xi)$, see Fig. 3. The wavelet-like properties enable a local, sparse reconstruction with a coefficients f_s only effectively contributing to $g(x)$ in a small neighborhood. By Eq. 11, the projected wavelets $\zeta_s^\alpha(x)$ are located at $2^{-j_s} P_x(S^{-1}k_s)$. Thus, only the wavelet coefficients defined at locations in a sheared tube in the u -direction above a location x' contribute to $g(x')$, see Fig. 8 left. We can therefore think of Eq. 15 as a wavelet representation of the image with the wavelets $\zeta_s^\alpha(x)$, although these are located at the non-canonical locations $P_x(2^{-j_s} S^{-1}k_s)$. In fact, with isotropic wavelets and $\alpha = 1$ the projection in Eq. 13 becomes

$$g(x) = \sum_{j,k_x} \underbrace{\left(\sum_{k_u} f_{j,k_x,k_u} \right)}_{f_{j,k_x}} \zeta_{j,k_x}^1(x), \quad (14a)$$

which is a standard, one dimensional wavelet representation of $g(x)$.

Next to the spatial position of $\psi_s(x)$, the contribution of f_s to $g(x)$ also depends on the orientation of $\psi_s(x)$, or, equivalently, on the corresponding $\beta_{j,n}^t$, cf. Eq. 12. As is apparent from Fig. 5, the magnitude of the reconstruction filters $\zeta_s^\alpha(x)$ is non-negligible only when the direction $S_\alpha^{-T} \xi_0$ overlaps the effective support of the wavelets in the frequency domain. When curvelet- or ridgelet-like wavelets are used, i.e. when $\hat{\psi}_s(\xi)$ has strong directional localization, then only a sheared wedge or a small number of wedges from the polar tiling of the frequency plane have effective support over the direction. Hence, only these directions need to be considered in the sum over s in the sheared Fourier slice equation in Eq. 13.

Our result relies on the use of polar wavelets that, through their definition in polar coordinates in frequency space, are compatible with the intrinsic structure of the projection, i.e. with a restriction to a line through the origin in the Fourier domain. With tensor product wavelets, e.g. using Daubechies-type, discrete wavelets, one would have a different, skew slicing through the axis-aligned frequency window for every α . The reconstruction kernel would then not

```

1 // Input: Sampled light field  $\ell$  in  $(x, y) \times (u, v)$  parameterization
2 Precomputation: ( $\ell$ )
3   // 1. Wavelet projection of light field in  $(x, u)$  and  $(y, v)$ 
4    $\ell_\psi = \{\ell_{sr}\} = \text{FWT}^2(L) \in \mathbb{R}^{|S| \times |S|}$ 
5   // 2. Computation of reconstruction filter, possibly sampling
6   // it for interpolation
7    $\zeta_s^\alpha(x) = \mathcal{F}_x^{-1} \left( \hat{\psi}_s(S_\alpha^{-T}(\xi_x, \xi_u))^T|_{\xi_u=0} \right)$ 
8 end
9 // Input: shear  $\alpha$ , resolution  $n$  for reconstruction
10 Reconstruction: ( $\alpha, n$ )
11   // 1. Determine locations for reconstruction
12    $x = \{ -2^{-j_{\max} - 1} N / \alpha, \dots, 2^{-j_{\max} - 1} N / \alpha \}$ 
13   // 2. Evaluate projection of sheared locations
14    $k_s^\alpha = 2^{j_s} P_x(S^{-1}k_s)$ 
15   // 3. Evaluate  $\zeta_s^\alpha(x - k_s^\alpha)$  for all  $x_i$  and  $k_s^\alpha$ 
16    $Z = \{\zeta_s^\alpha(x_i - k_s^\alpha)\}_{i,s} \in \mathbb{R}^{n \times |S|}$ 
17   // 4. Reconstruction of  $n \times n$  raw image
18    $I = Z \ell_\psi Z^T$ 
19 end

```

Algorithm 1: α -sheared image reconstruction from wavelet compressed representation (for single color channel).

have a closed form solution and, since the wavelets have no simple description, even determining them numerically would be difficult.

3.3 Imaging with the Sheared Local Fourier Slice Equation

We now return to refocused image reconstruction from the polar wavelet representation of a light field. Using the local Fourier slice equation and inserting Eq. 7 into Eq. 12 we obtain

$$I(x, y) = \sum_{(s,r) \in \mathcal{L}} \ell_{sr} \zeta_s^\alpha(x) \zeta_r^\alpha(y). \quad (15)$$

The $\zeta_s^\alpha(x)$ thus provide the reconstruction filters that implement α -refocused image reconstruction directly from the wavelet coefficients ℓ_{sr} of the light field, that is without the need to decompress. In practice, a displayable representation of an image is obtained by evaluating Eq. 15 for every pixel (possibly with multiple samples to increase the quality). We summarize the computations that are required for image reconstruction using Eq. 15 in Algorithm 1.

Eq. 15 can also be thought of as a separable wavelet representation of the image with the wavelets $\zeta_s^\alpha(x)$ and $\zeta_r^\alpha(y)$, although these are located at the non-canonical locations $P_x(2^{-j} S^{-1}k)$. Note that the spatial and directional locality $\zeta_s^\alpha(x)$ discussed in Sec. 3.2 immediately carries over to Eq. 15 and, for example, only ℓ_{sr} where $\hat{\psi}_s(\xi_x, \xi_u)$ and $\hat{\psi}_r(\xi_y, \xi_v)$ are oriented along the slicing direction contribute to the image $I(x, y)$, cf. again Fig. 5.

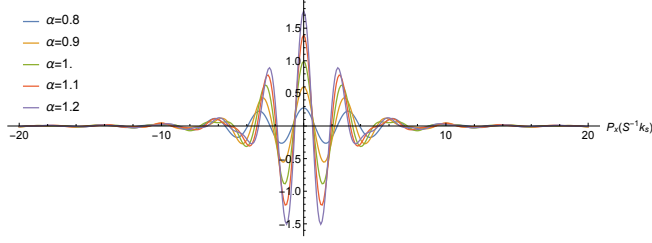


Fig. 7. Coupling coefficient γ_{sq} in Eq. 17 for $j_s = j_q$ and $k_q = 0$ as a function of $P_x(2^{-j}S^{-1}k_s)$.

3.4 Compressed Image Reconstruction

It is often useful to directly obtain the compressed representation of an image from a compressed light field, i.e. without first having to obtain a dense pixel representation as an intermediate step. We will show next how the result of Sec. 3.2 can be extended for this.

We assume that the light field is again provided in the polar wavelet representation in Eq. 6 so that the projected light field is given by Eq. 15. Assuming a separable wavelet basis $\psi_q^1(x)\psi_p^1(y)$ is used for the image, the corresponding expansion coefficients are given by

$$\begin{aligned} \ell_{qp} &= \left\langle I(x, y), \psi_q^1(x)\psi_p^1(y) \right\rangle \\ &= \sum_{(s,r) \in \mathcal{L}} \ell_{sr} \left\langle \zeta_s^\alpha(x), \psi_q^1(x) \right\rangle_x \left\langle \zeta_r^\alpha(y), \psi_p^1(y) \right\rangle_y. \end{aligned} \quad (16)$$

By introducing

$$\gamma_{sq} = \left\langle \zeta_s^\alpha(x), \psi_q^1(x) \right\rangle \quad (17)$$

we can write more compactly

$$\ell_{qp} = \sum_{(s,r) \in \mathcal{L}} \ell_{sr} \gamma_{sq} \gamma_{rp}. \quad (18)$$

When $\psi_q^1(x)$ and $\psi_p^1(y)$ are one dimensional, bandlimited “polar” wavelets that use the same radial window $\hat{h}(\xi_x)$ as in Sec. 2, then the γ -coefficients in Eq. 17 can be computed in closed form; the expressions are provided in the accompanying Mathematica code. By the compact support of the wavelets in the frequency domain, the γ_{sq} are then, for moderate α , non-negligible only when $\max(0, |j_q - 1|) \leq j_s \leq |j_q + 1|$; when $|\alpha - 1|$ is large then $\max(0, |j_q - 2|) \leq j_s \leq |j_q + 2|$ holds. A plot of the γ_{sq} as a function of $P_x(2^{-j}S^{-1}k_s)$ for different values of α and $j_s = j_q$ is provided in Fig. 7. As can be seen there, the coefficients have a shape similar to $\zeta_s^\alpha(x)$, since $\hat{\zeta}_s^\alpha(\xi)$ is essentially a smoothed box function, and in particular they have the same spatial decay.

A consequence of Eq. 18 is that sparsity in the wavelet representation of a reconstructed image is induced by sparsity in those of the light field. In particular, for fixed (q, p) only the ℓ_{sr} with $|k_q - P_x(S_\alpha^{-T}k_s)| \lesssim 2^{-j_q}$ and $|k_p - P_x(S_\alpha^{-T}k_r)| \lesssim 2^{-j_p}$ contribute to ℓ_{qp} , since the wavelets decay in space with dyadic dilation from level to level. Hence, when all ℓ_{sr} in the sheared tube above k_q and k_p are negligible, cf. Fig. 8, then also ℓ_{qp} is negligible. The coefficient ℓ_{qp} can also become small through cancellation, since both the ℓ_{sr} and γ_{sq} are signed. Intuitively, this happens, for example,

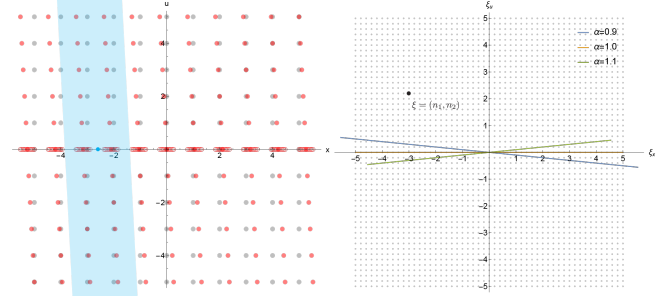


Fig. 8. *Left*: Original lattice of frame function locations (grey) and its shear (light red) for $\alpha = 0.95$. The projection (red circles) of the sheared lattice are on a denser grid, ensuring that the reconstruction filters ζ_s^α are on a grid that is sufficiently fine to meet the Nyquist criterion for the increased bandlimit that arises through the shearing. The bluish region schematically indicates the set of coefficients that determines the projection at the bluish location on the x -axis, indicating the locality of our approach. *Right*: The discrete Fourier transform in Fourier Slice Photography [Ng 2005] yields a signal on a discrete lattice of frequencies (grey). The evaluation directions $S^{-T}\xi_0$ does not lie on the lattice and the resampling introduces error.

when a region is defocused in the sheared projection and hence the wavelet coefficients on fine levels there have to be small. Such decay estimates are beyond the scope of the present paper and will be investigated elsewhere; existing result in this direction can be found in [Quinto 1993, 2007].

3.5 Computational Complexity of Image Reconstruction

In the following, we will analyze the computational complexity of Algo. 1. We assume that the reconstruction is performed for a region A , which is potentially a subset of the original image plane, with size $|A|$ and that R samples per unit are used. The input light field is assumed to have resolution $N_x \times N_x \times N_u \times N_u \times 3$ and we will ignore the apron that is used in practice to avoid boundary artifacts, since it is small and has a negligible effect on the complexity yet would make the analysis considerably more cumbersome.

Step 1 and Step 2 in Algo. 1 have negligible costs and we will therefore disregard them. For Step 3, the separable reconstruction kernel $\zeta_s^\alpha(x)\zeta_r^\alpha(y)$ has effective support $2^{-j_s}W \times 2^{-j_r}W$, where W is a window function-dependent constant, see Fig. 3. For each coefficient ℓ_{rs} it thus has to be evaluated K_R -times, with

$$K_R = c_\zeta 2^{-j_s - j_r} W^2 R \quad (19)$$

where c_ζ is the cost for one evaluation. Since at each level the resolution is reduced by a factor of 2 in each direction, the number of coefficients on level (j_s, j_r) in a dense representation is

$$|\mathcal{L}_{j_s, j_r}| = 6 \cdot 2^{-(j_{\max} - j_s)} 2^{-(j_{\max} - j_r)} N_x^2 N_u^2 T_{j_s} T_{j_r} |A| \quad (20)$$

where T_j is the number of different orientations on level j and the factor of 6 = 3 · 2 accounts for the three color channels as well as that we have two wavelet transforms in the separable representation of the light field.

$|\mathcal{L}_{j_s, j_r}|$ is reduced by two factors for the sheared projection. First, with anisotropic, curvelet-like frame functions only the α -sheared ones overlapping the slicing direction are required, cf. Fig. 5. These

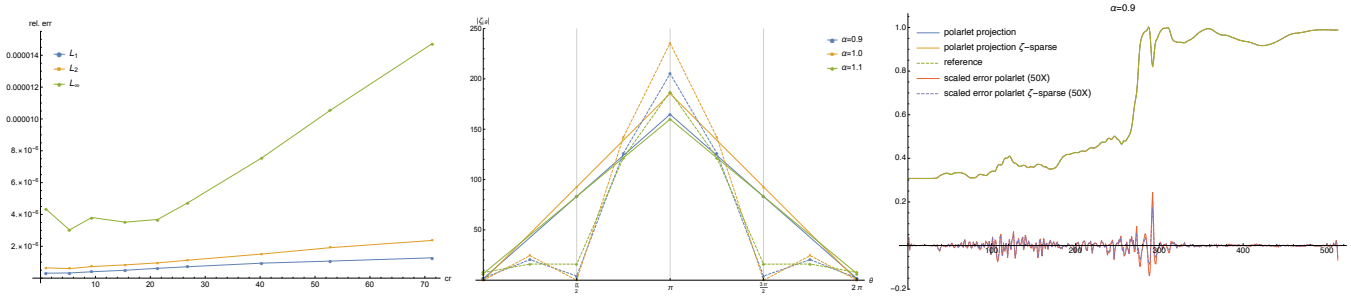


Fig. 9. Sheared projection with anisotropic, curvelet-like wavelets. *Left*: Reconstruction error as a function of the compression rate. *Middle*: $\|\zeta_{jkt}(x)\|$ as a function of t ; as expected the norm is non-negligible only when t is approximately aligned with the projection direction. *Right*: Reconstruction with all directions and only those where $\|\zeta_{jkt}(x)\|$ is non-negligible.

are of order one so that the number of coefficients contributing to the α -sheared projection is

$$|\mathcal{L}_{j_s, j_r}^\alpha| = 6 \cdot c \cdot 2^{-(j_{\max} - j_s)} 2^{-(j_{\max} - j_r)} N_x^2 N_u^2 |A|, \quad (21)$$

where $c = O(1)$. This effectively renders the redundancy of the frame irrelevant for the computational costs since a finer anisotropic tiling leads to a larger overcompleteness but also fewer functions overlapping the slicing direction. Second, for a faithful representation of the light field not all coefficients are required but a sparse set $\mathcal{L}_{j_s, j_r}^{\alpha, \epsilon}$ consisting of non-negligible ones with respect to a compression parameter ϵ (in the simplest case of hard thresholding, ϵ gives the threshold) suffices. The total cost of Eq. 15 is thus

$$K = K_R \cdot |\mathcal{L}_{j_s, j_r}^{\alpha, \epsilon}| = 6 \cdot c \cdot c_\zeta \cdot 2^{-j_s - j_r} W^2 R \mathcal{L}_{j_s, j_r}^\epsilon |A|. \quad (22)$$

Since c_ζ and W are basis dependent constants this becomes in big-O notation

$$O\left(2^{-j_s - j_r} |A| R |\mathcal{L}_{j_s, j_r}^\epsilon|\right). \quad (23)$$

Thus, the computational costs depend linearly on the size $|A|$ of the reconstruction region A as well as on the number of non-negligible coefficients $|\mathcal{L}_{j_s, j_r}^{\alpha, \epsilon}|$. The latter is typically well correlated with the visual complexity of an image.

Eq. 22 can also be written using the compression rate

$$\text{cr}_{j_s, j_r}^\epsilon = \frac{|\mathcal{L}_{j_s, j_r}^\epsilon|}{|\mathcal{L}_{j_s, j_r}^{\alpha, \epsilon}|} \quad (24)$$

that provides a relative measure of the sparsity of the compressed signal representation and that will be used in Sec. 4 when we analyze our numerical experiments. In terms of $\text{cr}_{j_s, j_r}^\epsilon$ we have

$$|\mathcal{L}_{j_s, j_r}^{\alpha, \epsilon}| = 2^{-(j_{\max} - j_s)} 2^{-(j_{\max} - j_r)} \frac{N_x^2 N_u^2}{\text{cr}_{j_r, j_s}^\epsilon} |A|. \quad (25)$$

Combining this with Eq. 19, the total cost of Eq. 15 is

$$C = C_R \cdot |\mathcal{L}_{j_s, j_r}^\epsilon| = 2^{-2j_{\max}} c_\zeta W^2 R \frac{N_x^2 N_u^2}{\text{cr}_{j_r, j_s}^\epsilon} |A| \quad (26)$$

where only the compression rate $\text{cr}_{j_r, j_s}^\epsilon$ still depends on the level (j_s, j_r) . In big-O notation this is

$$O(|A| R N_x^2 N_u^2 / \text{cr}_{j_r, j_s}^\epsilon). \quad (27)$$

The complexity of Ng's Fourier slice photography [Ng 2005] is, in our notation, $O(|A| R N_x^2)$. Although both works exploit that the projection becomes trivial in the Fourier domain, the spatial localization of the wavelets in our approach introduces again the directional resolution parameter N_u in Eq. 27. However, with the wavelets we also have a dependence on the compression rate cr . This can compensate for the N_u factor, depending on the rate cr that can be attained for the light field. Although theoretical characterizations of cr exist, see e.g. [Mallat 2009, Ch. 6, Ch. 9], these require technical assumptions about the signal that are difficult to precisely meet in practice. We will hence not pursue a further theoretical analysis here. Nonetheless, the practical utility of wavelets for the compression of image like signals, and hence that significant compression rates can be attained, is by now well established, as is evidenced by their use in the JPEG2000 standard.

3.6 Image Reconstruction Error

Ng [2005] discusses two sources of error for image reconstruction, namely roll off error and aliasing. We avoid roll-off error since our reconstruction kernels ζ_s^α are the exact ones for our analysis wavelets, which in turn provide a Parseval tight frame; when the wavelets are used up to level j_{\max} then all signals with bandlimit $2^j \pi$ can be represented exactly. Aliasing is of concern because the shearing can increase the bandlimit (the change in the bandlimit can be seen, e.g. in bottom right plot in Fig. 5). In our approach, this implies that for $\alpha < 1$ the ζ_s^α have a bandlimit beyond those of the original polar wavelets ψ_s . Consequently, they also need to be defined over a finer grid than the original wavelets to allow for perfect reconstruction. But, as shown in Fig. 8, left, the shearing also affects the grid over which the basis functions are defined and through this the ζ_s^α are inherently defined on a lattice that has the appropriate density.

Beyond roll off error and aliasing, a third source of error in fact arises in Ng's work [2005]. As depicted in Fig. 8, right, the discrete Fourier transform yields a lattice of discrete frequencies in the Fourier domain. Except in the trivial case when $\alpha = 1$, the slicing direction $S^{-T} \zeta_0$ does not lie on the lattice and the resampling onto a regular grid along the slicing direction provides an additional source of error. This error does not occur in our approach since our

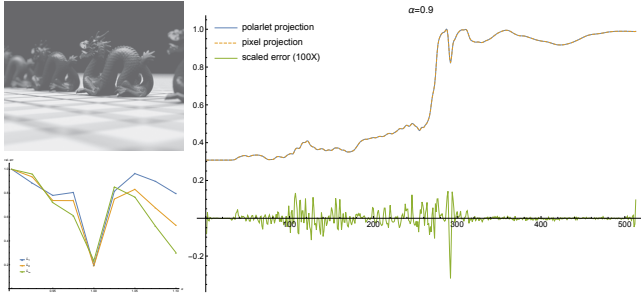


Fig. 10. *Right*: Sheared projection for the dragon image on the top left. *Bottom left*: Error of the projection as a function of the shearing angle α .

basis functions are defined in the continuous Fourier domain and we analytically compute the projection as a function of $\alpha \in \mathbb{R}$.

The main source of inaccuracies in our approach are in practice those introduced by a finite truncation of the basis functions or, equivalently, of the filter taps used in the fast transform. As discussed in Sec. 2, these can be ameliorated by using appropriate padding and filter sizes.

4 EXPERIMENTS

In this section we present experimental results that verify the practicality of the image reconstruction technique developed in the last section. A reference implementation as well as the raw images for most figures are provided in the supplementary material.

4.1 Implementation

To be able to easily vary the spatial and angular resolutions as well as the optical properties of the depicted scene, we implemented a custom light field film class for the pbrt renderer [Pharr and Humphreys 2010]. It directly records a light field in the two plane parameterization, applies the foreshortening factor of $\cos \theta^4 / F^2$ and also computes a depth map for the scene.

For image reconstruction we developed a Mathematica reference implementation of Algo. 1 (that is available in the supplementary material) and a basic C++ implementation. The $\zeta_S^\alpha(x)$ were sampled in a preprocessing step and interpolate at runtime; the error introduced through the interpolation was below 10^{-7} and thus negligible for optical applications. To avoid bias through post-processing we used one sample per pixel for image reconstruction and no interpolation filter on the image plane. Similarly, “reference” solutions were computed using naive projection in the pixel domain without filtering of the raw pixel data. For tone mapping a simple log-luminance transformation was used and none has been applied to error images. Numerical errors have also been computed on the high dynamic range data.

4.2 Simple experiments

To demonstrate the correctness of the sheared local Fourier slice equation as well as to gain some understanding of various conceptual aspects we performed experiments on two dimensional signals.

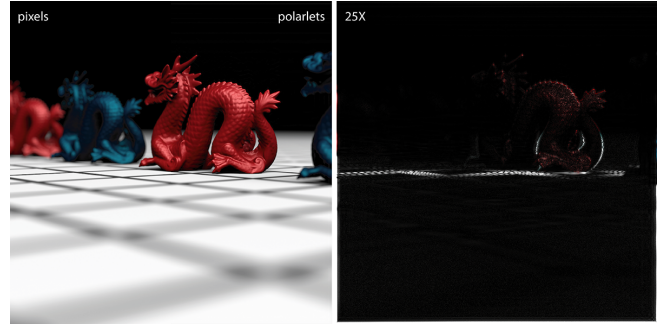


Fig. 11. Comparison between our approach and reconstruction in the pixel domain for $\alpha = 0.9$. The left image is split in the middle between the pixel reconstruction (left) and the polar wavelet reconstruction (right). The image on the right shows the error, magnified by a factor of 25. The error is on the level of those incurred by naïve slicing in the pixel domain.

Basic verification. We verified the correctness of the local Fourier slice equation using the sheared projection of a two dimensional Gaussian, for which an analytic solution exists. As shown in Fig 6, our reconstruction matches the analytic one very well with a maximum error on 1.86×10^{-6} . This is of the same order as the reconstruction error of the 2D input signal, and hence attributable to inaccuracies in the forward transform yielding the wavelet coefficients.

To obtain insights on the behavior of our technique for “natural images” as well as to understand the effect of α we considered a monochromatic dragons scene image, cf. Fig. 10, top left. The results in Fig. 10, right, demonstrate that our approach yields errors much smaller than what can be perceived visually and on the same order as differences that result with different reconstruction kernels for the pixel domain projection. The graph in the bottom left of Fig. 10 shows that the error does not significantly increase as α changes, with the reduction for $\alpha > 1$ resulting from the reduced bandlimit, and corresponding oversampling, that happens in this regime.

Sparsity and Directionality. For the dragon scene image we also studied the effect of sparsity as well as the gains that are possible using oriented, curvelet-like frame functions. The left plot in Fig. 9 shows the error as a function of the compression rate with hard thresholding used to obtain the sparse representation. As one would expect for a wavelet representation, very accurate reconstructions are possible with a small fraction of the original storage requirements. Furthermore, the error increases smoothly with the compression rate. The middle plot in Fig. 9 depicts $\|\zeta_{jkt}(x)\|$ as a function of the orientation of the wavelets. Because of the localized support of the directional wavelets in the frequency domain, cf. Fig. 5, only $\zeta_S(x) = \zeta_{jkt}(x)$ whose orientation t matches the slicing direction $S_\alpha^{-T} \xi_0$ are non-negligible. Since α does not fundamentally change the direction, some orientations are irrelevant, e.g. $t \leq \pi/2$ and $t \geq 3\pi/2$ in the plot. Importantly, this implies that the frame coefficients for the negligible orientations do not have to be stored, even if these are above an ϵ -threshold. $\|\zeta_{jkt}(x)\|$ can hence be understood as a signal independent form of sparsification. The right

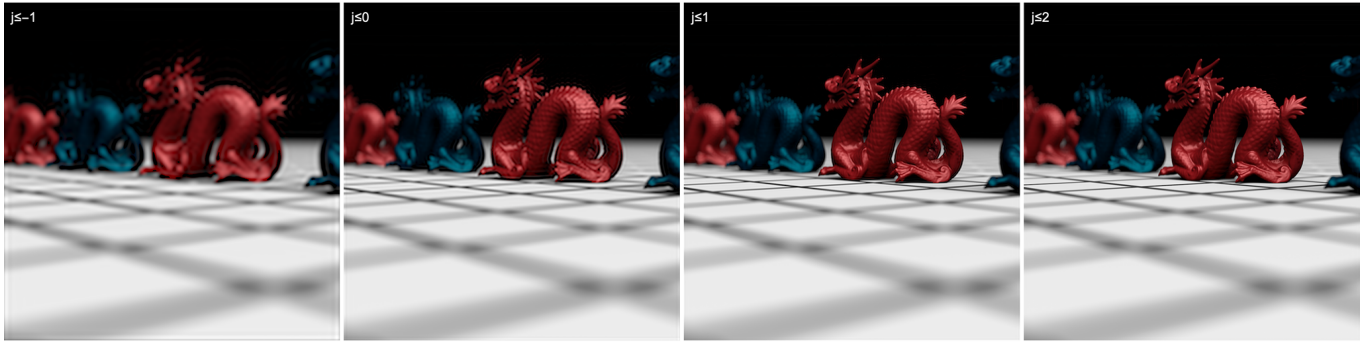


Fig. 12. Reconstructions with subsets of all wavelet levels, demonstrating that not all are required to obtain acceptable reconstructions. Furthermore, the error increases gracefully as the number of levels decreases. The contribution by the individual levels is shown in Fig. 15.

plot in Fig. 9 verifies that orientations far from the projection direction do not have to be taken into account for reconstruction, i.e. the reconstruction error is sufficiently small when these are ignored.

4.3 Image reconstruction

To demonstrate the practicality of Algo. 1 we generated light fields for a dragon scene and a villa interior. All experiments were performed with $1024 \times 1024 \times 33 \times 33 \times 3$ RGB data sets and we used two to three wavelet levels (because of the limited resolution in the angular dimension).

Refocusing. A refocused reconstruction of an image is provided in Fig. 11. The comparison to the projection in the pixel domain, also shown in the image, verifies that our result is visually indistinguishable and that the differences between both are on the order of what one would obtain with different reconstruction kernels for projection in the pixel domain.

Fig. 12 shows reconstructions with only a subset of levels and Fig. 15 the contribution made by the different levels. It can be seen that the error increases gracefully as one disregards finer levels with the reconstructed images becoming smoother but largely without objectionable artifacts, although some ringing can be observed for $j \leq -1$ and $j \leq 0$ in the in-focus region. Since a reconstruction with a subset of levels is considerably cheaper, requiring only 0.098%, 1.72%, 13.43% of the computation time for all levels for $j \leq -1$, $j \leq 0$, and $j \leq 1$ for the whole image, respectively, substantial savings for out-of-focus regions are possible when a depth map is known.

Sparsity. Fig. 14 compares reconstructed images when sparsity in the wavelet representation of the light field is exploited. In accordance with Fig. 9, the storage requirements can be considerably reduced without a visual degradation of the images. Furthermore, when the error becomes visible then it amounts to a lack of high frequency details but again largely without objectionable artifacts (image sequences as a function of the compression rate are provided in the supplementary material).

All-in-focus reconstruction. Fig. 16, right, shows a reconstruction of the dragons scene as well as of the checkerboard ground plane with a depth dependent α value so that the entire scene is in focus. Slight artifacts are visible around the dragon silhouettes, since we

do not take the varying support of the $\zeta_s^\alpha(x)$ into account and only sample the depth map at the location of the reconstruction kernels.

Performance. Fig. 13 shows the relative execution time as a function of the compression rate. Although our implementation is not particularly optimized and we only use Eigen for the sparse wavelet representation, they demonstrate that sparsity can lead to a substantial reduction in computation time. The plots also show the time decreases approximately as $1/cr$, as one would expect from our analysis of the computational complexity in Sec. 3.5, see in particular Eq. 27.

The absolute computation time of image reconstruction is currently on the order of a minute for a $1024 \times 1024 \times 33 \times 33 \times 3$ light field data set. The same time is approximately required to project a light field data set into the wavelet representation, although, again, our implementation is not optimized at the moment.

4.4 Discussion

Our experimental results demonstrate the practical viability of Algo. 1 to reconstruct refocused images from the wavelet representation of a light field. In particular, we verified that high fidelity images can be obtained from a sparse, compressed representation and that the error increases gracefully with the compression rate. Our results also show that the sparsity can lead to a significant reduction in the computation time. Furthermore, Algo. 1 can be parallelized by performing the reconstruction for each pixel independently, which makes it directly amenable to a GPU implementation. There, one

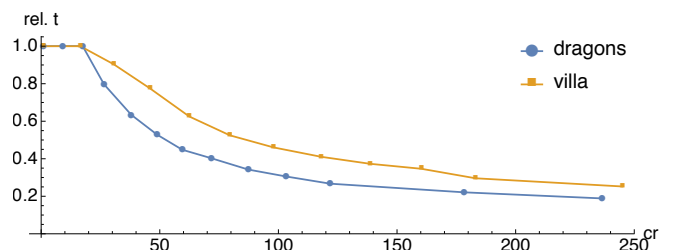


Fig. 13. Relative execution time as function of sparsity for the scenes in Fig. 14.

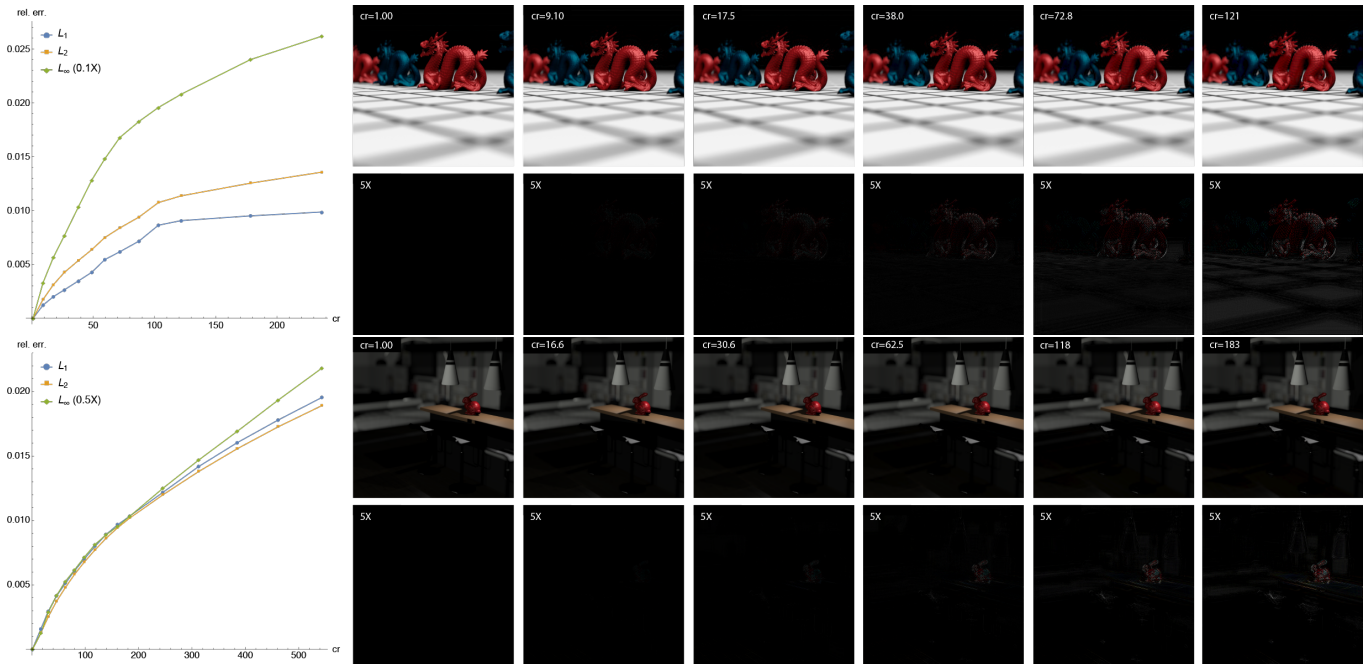


Fig. 14. Reconstruction error as a function of the compression rate cr . The relative errors on the left are with respect to the respective norms in the uncompressed image and the second and fourth rows on the right show difference images compared to the uncompressed reference, magnified by a factor of five. The results demonstrate that a reconstruction from the compressed light field is feasible and beneficial. Even with very high compression rates, such as in the right most image column, the errors manifest itself as missing high frequency details, e.g. on the back of the red dragon, but there are largely no disruptive visual artifacts. Animations for the reconstructed image as well as the difference images as a function of compression rate are provided in the supplementary material.

could also take advantage of half-precision, which is sufficient to obtain artifact free images and would also provide benefits on the embedded processors typically available in cameras.

Fig. 16 showed first results on the reconstruction of all-focus images from the compressed wavelet representation. While currently not artifact free when the depth map contains discontinuities, the results verify the potential of our approach to obtain all-focus images, which is not possible using Fourier slice photography where a fixed α has to be used. To remove the current artifacts, the depth map needs to be preprocessed in a mip-map-like manner so that an average depth can be sampled at each wavelet level and it might also be necessary to restrict the support of wavelets at depth discontinuities.

Although we performed experiments with both isotropic and curvelet-like, anisotropic polar wavelets, more work is required to understand the best trade-off between the higher redundancy of directional representations and the increased sparsity that these provide. Towards this end, it would be beneficial to analyze the fidelity of reconstructed images across a large set of light fields, including measured ones. While our synthetic ones were not perfect and suffer in particular from Monte Carlo noise, measured light fields have different artifacts and it would hence be important to experimentally validate the performance of our approach on these.

5 CONCLUSION

In this paper, we presented a sheared local Fourier slice equation and applied it to post-capture refocus of light fields from their compressed wavelet representation. This enables a significant reduction in storage requirements without having to reconstruct a dense representation of the light field for image synthesis. We also analyzed the computational complexity of our technique, which showed that it depends linearly on the number of nonzero coefficients and the size of the reconstruction region. More work is required, however, to develop our technique to a practical alternative to existing approaches. For example, it needs to be investigated if the increased sparsity of directional, curvelet-like representations outweighs the higher costs for evaluating these. We also did not consider measured light fields. Although these pose no conceptual challenge, the optimal parameter settings might differ from those for synthetic ones. The reconstruction of all-focus images with our local Fourier slice equation also requires further work, cf. Fig. 16.

Our current approach for image reconstruction exploits the separability of the refocusing problem so that two dimensional polar wavelets are sufficient. This is sub-optimal concerning the compression rates that can be attained for the light field and also since one obtains a separable wavelet representation for the reconstructed image. With 4D polar wavelets, which can be constructed as an extension of the polar wavelets used in the present work, cf. [Ward and Unser 2014], the entire light field could be represented in one wavelet basis and the projection of the data would then yield two

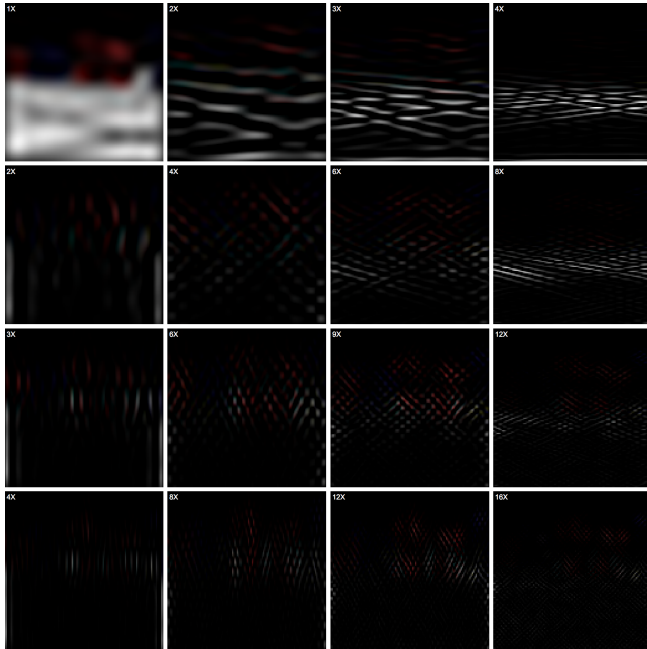


Fig. 15. For the dragon scene in Fig. 12, contributions by different levels for $j_s = -1, \dots, 2$ (columns) and $j_r = -1, \dots, 2$ (rows) magnified by the factor shown in the inset. The results verify that very fine levels can be omitted when performance is of importance.

dimensional, curvelet-like polar wavelets. In our opinion, this is both theoretically and practically an interesting direction for future work.

We believe that the polar wavelet representation of images and light fields could also be beneficial for other applications. For instance, the feature-aware resizing of Gastal and Oliveira [2017] is naturally formulated in polar coordinates and could also be performed directly in the compressed representation. The polar wavelet representation of light fields might also be beneficial for learning techniques since it reduces the redundancy in the data while respecting the intrinsic structure that is required for image reconstruction.

ACKNOWLEDGMENTS

First ideas for the project were developed while the author was a post-doc in Marc Alexa's computer graphics group at TU Berlin. He would also like to thank Eugene Fiume for continuing support.

REFERENCES

- A. Aggoun. 2006. A 3D Dct Compression Algorithm For Omnidirectional Integral Images. In *2006 IEEE International Conference on Acoustics Speed and Signal Processing Proceedings*, Vol. 2. IEEE, II-517–II-520. <https://doi.org/10.1109/ICASSP.2006.1660393>
- A. Aggoun and M. Mazri. 2008. Wavelet-based compression algorithm for still omnidirectional 3d integral images. *Signal, Image and Video Processing* 2, 2 (jun 2008), 141–153. <https://doi.org/10.1007/s11760-007-0044-1>
- G. Alves, M. P. Pereira, M. B. de Carvalho, F. Pereira, C. L. Pagliari, V. Testoni, and E. A.B. da Silva. 2018. A Study on the 4D Sparsity of JPEG Pleno Light Fields Using the Discrete Cosine Transform. In *2018 25th IEEE International Conference on Image Processing (ICIP)*. IEEE, 1148–1152. <https://doi.org/10.1109/ICIP.2018.8451583>
- E. Candès and D. L. Donoho. 2004. New Tight Frames of Curvelets and Optimal Representations of Objects with Piecewise \mathcal{S}^2 Singularities. *Communications on*

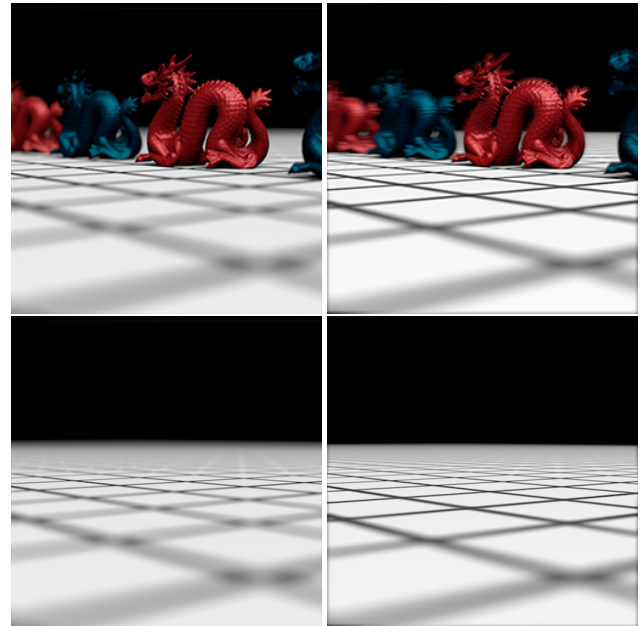


Fig. 16. Reconstructions for $\alpha = 1.0$ (left) and with α determined based on a depth map (right) to obtain all-focus reconstructions (α is restricted to $[0.6, 1.4]$ which leaves the region nearest to the camera still out of focus). Because we use only a single high resolution depth map and do not consider the variable support of the reconstruction kernels ζ_s^α as a function of level, artifacts are visible around the silhouettes of the dragons.

- Pure and Applied Mathematics* 57, 2 (feb 2004), 219–266. <https://doi.org/10.1002/cpa.10116>
- E. J. Candès and D. L. Donoho. 1999. Ridgelets: A Key to Higher-Dimensional Intermittency? *Royal Society of London Philosophical Transactions Series A* 357 (1999), 2495–+.
- E. J. Candès and D. L. Donoho. 2005a. Continuous curvelet transform: I. Resolution of the Wavefront Set. *Applied and Computational Harmonic Analysis* 19, 2 (sep 2005), 162–197. <https://doi.org/10.1016/j.acha.2005.02.003>
- E. J. Candès and D. L. Donoho. 2005b. Continuous curvelet transform: II. Discretization and Frames. *Applied and Computational Harmonic Analysis* 19, 2 (sep 2005), 198–222. <https://doi.org/10.1016/j.acha.2005.02.004>
- J.-X. Chai, S.-C. Chan, H.-Y. Shum, and X. Tong. 2000. Plenoptic Sampling. In *Proceedings of the 27th annual conference on Computer graphics and interactive techniques - SIGGRAPH '00*. ACM Press, New York, New York, USA, 307–318. <https://doi.org/10.1145/344779.344932>
- C. Conti, P. T. Kovacs, T. Balogh, P. Nunes, and L. D. Soares. 2014. Light-field video coding using geometry-based disparity compensation. In *2014 3DTV-Conference: The True Vision - Capture, Transmission and Display of 3D Video (3DTV-CON)*. IEEE, 1–4. <https://doi.org/10.1109/3DTV.2014.6874724>
- F. Dai, J. Zhang, Y. Ma, and Y. Zhang. 2015. Lenselet image compression scheme based on subaperture images streaming. In *2015 IEEE International Conference on Image Processing (ICIP)*. IEEE, 4733–4737. <https://doi.org/10.1109/ICIP.2015.7351705>
- D. L. Donoho. 2000. Orthonormal Ridgelets and Linear Singularities. *SIAM Journal on Mathematical Analysis* 31, 5 (aug 2000), 1062. <https://doi.org/10.1137/S0036141098344403>
- F. Durand, N. Holzschuch, C. Soler, E. Chan, and F. Sillion. 2005. A Frequency Analysis of Light Transport. *ACM Transactions on Graphics (Proceedings of SIGGRAPH 2005)* 24 (2005).
- W. T. Freeman and E. H. Adelson. 1991. The design and use of steerable filters. *IEEE Transactions on Pattern Analysis and Machine Intelligence* 13, 9 (1991), 891–906. <https://doi.org/10.1109/34.93808>
- E. S. L. Gastal and M. M. Oliveira. 2017. Spectral remapping for image downscaling. *ACM Transactions on Graphics* 36, 4 (jul 2017), 1–16. <https://doi.org/10.1145/3072959.3073670>
- S. J. Gortler, R. Grzeszczuk, R. Szeliski, and M. F. Cohen. 1996. The Lumigraph. In *SIGGRAPH '96: Proceedings of the 23rd annual conference on Computer graphics and*

- interactive techniques*. ACM, New York, NY, USA, 43–54. <https://doi.org/10.1145/237170.237200>
- I. Ihrke, J. Restrepo, and L. Mignard-Debise. 2016. Principles of Light Field Imaging: Briefly revisiting 25 years of research. *IEEE Signal Processing Magazine* 33, 5 (sep 2016), 59–69. <https://doi.org/10.1109/MSP.2016.2582220>
- N. K. Kalantari, T.-C. Wang, and R. Ramamoorthi. 2016. Learning-based view synthesis for light field cameras. *ACM Transactions on Graphics* 35, 6 (nov 2016), 1–10. <https://doi.org/10.1145/2980179.2980251>
- S. Kundu. 2012. Light field compression using homography and 2D warping. In *2012 IEEE International Conference on Acoustics, Speech and Signal Processing (ICASSP)*. IEEE, 1349–1352. <https://doi.org/10.1109/ICASSP.2012.6288140>
- C. Lessig. 2018a. A local Fourier slice equation. *Optics Express* 26, 23 (nov 2018), 29769. <https://doi.org/10.1364/OE.26.029769>
- C. Lessig. 2018b. Polar Wavelets in Space. *Submitted to IEEE Signal Processing Letters* (2018). arXiv:1805.02061 <https://arxiv.org/abs/1805.02061>
- A. Levin, W. T. Freeman, and F. Durand. 2008. Understanding Camera Trade-Offs through a Bayesian Analysis of Light Field Projections. In *Computer Vision and Pattern Recognition (CVPR) 2008*. Springer Berlin Heidelberg, Berlin, Heidelberg, 88–101. https://doi.org/10.1007/978-3-540-88693-8_7
- M. Levoy and P. Hanrahan. 1996. Light Field Rendering. In *SIGGRAPH '96: Proceedings of the 23rd annual conference on Computer graphics and interactive techniques*. ACM, New York, NY, USA, 31–42. <https://doi.org/10.1145/237170.237199>
- M. Levoy, R. Ng, A. Adams, M. Footer, and M. Horowitz. 2006. Light Field Microscopy. In *ACM Trans. Graph. (Proceedings of ACM SIGGRAPH 2006)*, Vol. 25. ACM Press, New York, New York, USA, 924. <https://doi.org/10.1145/1179352.1141976>
- C.-K. Liang and R. Ramamoorthi. 2015. A Light Transport Framework for Lenslet Light Field Cameras. *ACM Transactions on Graphics* 34, 2 (mar 2015), 1–19. <https://doi.org/10.1145/2665075>
- S. G. Mallat. 2009. *A Wavelet Tour of Signal Processing: The Sparse Way* (third ed. ed.). Academic Press.
- R. Ng. 2005. Fourier Slice Photography. *ACM Transactions on Graphics* 24, 3 (jul 2005), 735. <https://doi.org/10.1145/1073204.1073256>
- R. Ng, M. Levoy, M. Brédif, G. Duval, M. Horowitz, and P. Hanrahan. 2005. Light field photography with a hand-held plenoptic camera. (2005).
- P. Perona. 1991. Deformable kernels for early vision. In *Proceedings. 1991 IEEE Computer Society Conference on Computer Vision and Pattern Recognition*. IEEE Comput. Soc. Press, 222–227. <https://doi.org/10.1109/CVPR.1991.139691>
- M. Pharr and G. Humphreys. 2010. *Physically Based Rendering: From Theory to Implementation* (second ed.). Morgan Kaufmann Publishers Inc., San Francisco, CA, USA.
- J. Portilla and E. P. Simoncelli. 2000. A Parametric Texture Model Based on Joint Statistics of Complex Wavelet Coefficients. *International Journal of Computer Vision* 40, 1 (2000), 49–70. <https://doi.org/10.1023/A:1026553619983>
- E. T. Quinto. 1993. Singularities of the X-Ray Transform and Limited Data Tomography in \mathbb{R}^2 and \mathbb{R}^3 . *SIAM Journal on Mathematical Analysis* 24, 5 (sep 1993), 1215–1225. <https://doi.org/10.1137/0524069>
- E. T. Quinto. 2007. Local algorithms in exterior tomography. *J. Comput. Appl. Math.* 199, 1 (feb 2007), 141–148. <https://doi.org/10.1016/J.CAM.2004.11.055>
- L. Shi, H. Hassanieh, A. Davis, D. Katabi, and F. Durand. 2014. Light Field Reconstruction Using Sparsity in the Continuous Fourier Domain. *ACM Transactions on Graphics* 34, 1 (dec 2014), 1–13. <https://doi.org/10.1145/2682631>
- E. P. Simoncelli and W. T. Freeman. 1995. The steerable pyramid: a flexible architecture for multi-scale derivative computation. In *Proceedings., International Conference on Image Processing*, Vol. 3. IEEE Comput. Soc. Press, 444–447. <https://doi.org/10.1109/ICIP.1995.537667>
- M. Unser and N. Chenouard. 2013. A Unifying Parametric Framework for 2D Steerable Wavelet Transforms. *SIAM Journal on Imaging Sciences* 6, 1 (jan 2013), 102–135. <https://doi.org/10.1137/120866014>
- M. Unser, N. Chenouard, and D. Van De Ville. 2011. Steerable Pyramids and Tight Wavelet Frames in $\mathbb{L}_2(\mathbb{R}^d)$. *IEEE Transactions on Image Processing* 20, 10 (oct 2011), 2705–2721. <https://doi.org/10.1109/TIP.2011.2138147>
- M. Unser and D. Van De Ville. 2010. Wavelet Steerability and the Higher-Order Riesz Transform. *IEEE Transactions on Image Processing* 19, 3 (mar 2010), 636–652. <https://doi.org/10.1109/TIP.2009.2038832>
- K. Venkataraman, D. Lelescu, J. Duparré, A. McMahon, G. Molina, P. Chatterjee, R. Mullis, and S. Nayar. 2013. PiCam: an ultra-thin high performance monolithic camera array. *ACM Transactions on Graphics* 32, 6 (nov 2013), 1–13. <https://doi.org/10.1145/2508363.2508390>
- A. Vieira, H. Duarte, C. Perra, L. Tavora, and P. Assuncao. 2015. Data formats for high efficiency coding of Lytro-Illum light fields. In *2015 International Conference on Image Processing Theory, Tools and Applications (IPTA)*. IEEE, 494–497. <https://doi.org/10.1109/IPTA.2015.7367195>
- I. Viola, M. Rerabek, and T. Ebrahimi. 2017. Comparison and Evaluation of Light Field Image Coding Approaches. *IEEE Journal of Selected Topics in Signal Processing* 11, 7 (oct 2017), 1092–1106. <https://doi.org/10.1109/JSTSP.2017.2740167>

- J. P. Ward and M. Unser. 2014. Harmonic singular integrals and steerable wavelets in $\mathbb{L}_2(\mathbb{R}^d)$. *Applied and Computational Harmonic Analysis* 36, 2 (mar 2014), 183–197. <https://doi.org/10.1016/J.ACHA.2013.03.006>
- B. Wilburn, N. Joshi, V. Vaish, E.-V. Talvala, E. Antunez, A. Barth, A. Adams, M. Horowitz, and M. Levoy. 2005. High Performance Imaging Using Large Camera Arrays. *ACM Trans. Graph. (Proceedings of ACM SIGGRAPH 2005)* (2005). <https://graphics.stanford.edu/papers/CameraArray/>
- G. Wu, B. Masia, A. Jarabo, Y. Zhang, L. Wang, Q. Dai, T. Chai, and Y. Liu. 2017. Light Field Image Processing: An Overview. *IEEE Journal of Selected Topics in Signal Processing* 11, 7 (oct 2017), 926–954. <https://doi.org/10.1109/JSTSP.2017.2747126>
- Z. Xu, K. Sunkavalli, S. Hadap, and R. Ramamoorthi. 2018. Deep image-based relighting from optimal sparse samples. *ACM Transactions on Graphics* 37, 4 (jul 2018), 1–13. <https://doi.org/10.1145/3197517.3201313>
- Y. Yoon, H.-G. Jeon, D. Yoo, J.-Y. Lee, and I. S. Kweon. 2015. Learning a Deep Convolutional Network for Light-Field Image Super-Resolution. In *2015 IEEE International Conference on Computer Vision Workshop (ICCVW)*. IEEE, 57–65. <https://doi.org/10.1109/ICCVW.2015.17>

A SPATIAL REPRESENTATION OF RECONSTRUCTION FILTERS ζ_s^α

When $\hat{h}(\xi)$ is the wavelet window from the steerable pyramid, the $\zeta_s^{\alpha, m}(x)$ in Eq. 12 are given by

$$\begin{aligned} \zeta_s^{\alpha, n}(x) &= \frac{1}{2\sqrt{2}x} \pi^{-\frac{\log(2)+i\pi}{\log(4)}} \left(\left(1 - \frac{1}{\alpha}\right)^2 \alpha^2 + 1 \right)^{-\frac{i\pi}{\log(16)}} \\ &\times e^{-in(\pi - \tan^{-1}((1 - \frac{1}{\alpha})\alpha))} \left(\alpha^2 x^2 \right)^{-\frac{i\pi}{\log(4)}} \\ &\times \pi^{\frac{i\pi}{\log(2)}} A + \left(\left(1 - \frac{1}{\alpha}\right)^2 \alpha^2 + 1 \right)^{\frac{i\pi}{\log(4)}} B \end{aligned}$$

where

$$A = (-i\alpha x)^{\frac{i\pi}{\log(2)}} (i\alpha x)^{\frac{i\pi}{\log(4)}} \left(e^{i\pi n} (D_4^- - D_1^-) - (D_4^+ - D_1^+) \right)$$

$$B = e^{i\pi n} (i\alpha x)^{\frac{i\pi}{\log(4)}} (D_4^- - D_1^-) - (-i\alpha x)^{\frac{i\pi}{\log(4)}} (D_4^+ - D_1^+)$$

and

$$D_d^\pm = \Gamma \left(1 \pm \frac{i\pi}{\log(4)}, \pm \frac{i\pi x \alpha}{d \sqrt{\left(1 - \frac{1}{\alpha}\right)^2 \alpha^2 + 1}} \right).$$